Available online at www.sciencedirect.com
ScienceDirect
Trans. Nonferrous Met. Soc. China 29(2019) 287−295
Transactions of Nonferrous Metals Society of China
www.tnmsc.cn

Effect of welding sequence on residual stress and deformation of 6061-T6 aluminium alloy automobile component

Jie YI[1,2,3], Jian-ming ZHANG[1,3], Shu-fen CAO[1,3], Peng-cheng GUO[1,3]

1. State Key Laboratory of Advanced Design and Manufacture for Vehicle Body, Hunan University, Changsha 410082, China;
2. School of Mechanical Engineering, Hunan Industry Polytechnic, Changsha 410208, China;
3. College of Mechanical and Vehicle Engineering, Hunan University, Changsha 410082, China

Received 7 May 2018; accepted 19 November 2018

Abstract: Four different welding sequences of double-pulse MIG welding were conducted for 6061-T6 aluminum alloy automobile bumpers by using nonlinear elastoplasticity finite element method based on ABAQUS software. The post-welding residual stress and deformation were definitely different among the four welding sequences. The results showed that the highest temperature in Solution A was approximately 200 °C higher than the melting point of base metal. High residual stress was resulted from this large temperature gradient and mainly concentrated on the welding vicinity between beam and crash box. The welding deformation primarily occurred in both of the contraction of two-ends of the beam and the self-contraction of crash box. Compared with other welding sequences, the residual stress in Solution A was the smallest, whereas the welding deformation was the largest. However, the optimal sequence was Solution B because of the effective reduction of residual stress and good assembly requirements.

Key words: double-pulse MIG welding; welding sequence; welding residual stress; welding deformation; optimal solution

1 Introduction

As the important components in the automotive body safety structure, bumper is indirectly used to protect drivers and passengers by carrying loads and absorbing energy in the low-speed collision. In comparison with traditional steel component, the bumper made of aluminum alloy can not only significantly decrease the mass by 40%−70% but also increase the energy absorbed in a collision [1,2]. Generally, the automobile bumper assembly consists of a beam, a left crash box and a right crash box, which are welded together. In this study, a double-pulse MIG welding was applied to a thin-plate bumper welding, which produced high-quality aluminum alloy welds and effectively controlled bumper deformation. This welding process with the useful control of heat input could also improve the welded joint performance and could produce a good fish-scale shape weld appearance [3].

However, the bumper made up of an aluminum alloy thin-walled cavity structure is instantly, locally heated and air-cooled. This process may produce high local stress and deformation and affect the quality and accuracy of the bumper. That is due to the high specific heat capacity, thermal conductivity coefficient and linear expansion coefficient of aluminum alloy [4]. Thus, welding residual stress and deformation can be effectively reduced by optimizing the welding sequence on account of the welded structures with multiple welds. To avoid the complexity of the practical welding process and the high cost of conducting welding tests on complicated structures, many scholars have used the finite element numerical simulation method to simulate the temperature delivery and stress−strain behavior in welding the complicated structures. Afterwards, effective predictions were made for the overall stress distribution and deformation of the welds, and the optimal welding processes were obtained through optimization of welding sequences. In the research of SATTARI-FAR and JAVADI [5], the finite element method was used to study the effects of nine different welding sequences on the

Foundation item: Projects (31665004, 31715011) supported by the Open Fund of State Key Laboratory of Advanced Design and Manufacture for Vehicle Body, Hunan University, China; Project (15C0450) supported by the Educational Commission of Hunan Province of China
Corresponding author: Jie YI; Tel: +86-15111270111; E-mail: 444623777@qq.com
DOI: 10.1016/S1003-6326(19)64938-1

residual stress of the welds on thin-walled octagonal tube plates. The results showed that the initial residual stress on the welds and their vicinities did not affect the final distribution of the residual stress and that a sequence combining step-by-step welding and symmetrical welding effectively reduced the residual stress on the welds. FU et al [6] conducted the simulation and experimental study about TIG welding on segmental butt joints of V-shaped joints on two circular tubes to obtain an optimal welding sequence and reduce the welding residual stress and deformation effectively.

Although the optimization of welding sequence has been reported to date, the welding structures were relatively simple. Mostly, these studies are focused on the effects of welding sequences on welding stress and deformation of plates and circular structures; few focused on the simulation of long sections with two-ends undergoing girth welding or the optimization of relevant welding sequences. In this work, based on the thermal elastoplastic finite element method, the process of conducting girth welding on the crash boxes at two-ends of an automobile bumper was analyzed to obtain residual stress distribution and overall deformation. Four typical welding sequences were discussed and the optimal one was put forward to effectively control the welding stress and deformation.

2 Establishment of welding finite element model

2.1 Finite element mesh model of bumper

Figure 1 shows the entire structure of an automobile front bumper assembly. The thickness of the section is 2 mm. The cross member is a multi-cell extruded section and its dimensions are 100 mm × 30 mm × 1100 mm. The cross-section of the crash box is relatively complicated. In the welding simulation, the cross member was simplified to an 80 mm × 70 mm square thin-walled section. As the welding deformation of the front bumper assembly was mainly concentrated on the beam, the influence of the simplification on the optimization results can be ignored. Girth full welding was used to weld along the edge of the crash box. The bumper assembly had 8 welds in total, each of which was 600 mm. A 3D finite element model was set up, as shown in Fig. 2. To increase calculation accuracy and efficiency, a smaller element size (2 mm × 2 mm × 0.2 mm) was adopted in the welds and a larger element size (10 mm × 2 mm × 0.2 mm) was used in their vicinities. An 8-node DC3D8 thermal element was used during the temperature simulation, whereas a C3D8R structural element was adopted during the stress−strain simulation.

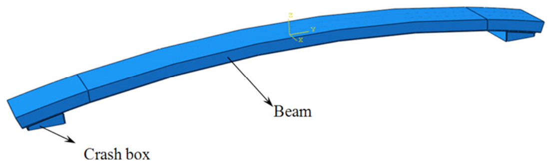

Fig. 1 Bumper geometric model

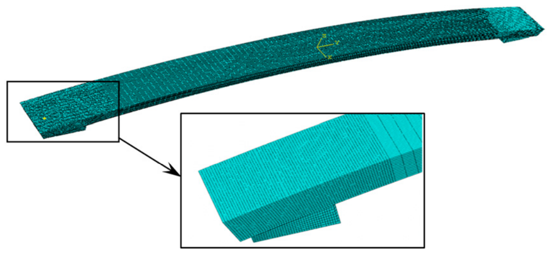

Fig. 2 3D finite element model for bumper

2.2 Heat source model

Heat source model affects the simulation of the welding process significantly [7]. In this study, the heat source function model with double-ellipsoidal distribution was used, as shown in Fig. 3, to simulate the welding process of MIG welding flexibly. This model used two distinct quarter ellipsoids, to approximate the front and back halves of the arc, and the corresponding heat input was distributed in the two ellipsoids. The process focused on the effect of the arc in the welding process as well as the heat changes along thickness direction. Thus, this method could accurately manifest the effect produced by arc stiffness during welding.

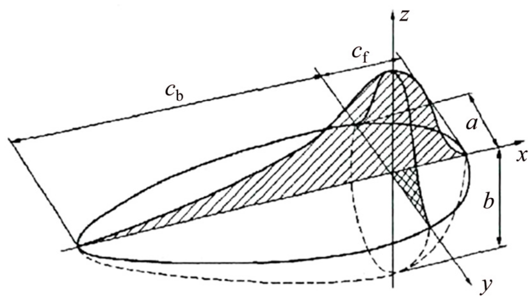

Fig. 3 Schematic diagram of double-ellipsoidal volumetric heat source [8]

On the front half of the ellipsoid, the heat input distribution can be expressed as follows [8]:

$$q(x,y,z)=\frac{6\sqrt{3}f_f Q}{abc_f\pi\sqrt{\pi}}\exp\left[-3\left(\frac{x^2}{c_f^2}+\frac{y^2}{a^2}+\frac{z^2}{b^2}\right)\right] \tag{1}$$

where a, b and c_f are the shape parameters of the heat input, respectively; Q is the thermal input power; f_f is the energy distribution coefficient of the front half of the ellipsoid.

On the back half of the ellipsoid, the heat input distribution can be expressed as follows [8]:

$$q(x,y,z)=\frac{6\sqrt{3}f_bQ}{abc_b\pi\sqrt{\pi}}\exp\left[-3\left(\frac{x^2}{c_b^2}+\frac{y^2}{a^2}+\frac{z^2}{b^2}\right)\right] \tag{2}$$

where c_b is the shape parameter the heat input, and f_b is the energy distribution coefficient of the back half of the ellipsoid. Here, $f_f+f_b=2$. In general, $f_f=0.4$ and $f_b=1.6$, which are employed for the analysis optimization.

Double-pulse MIG welding can be considered as the modulation of high frequency pulse based on low frequency pulse and the superposition of high frequency pulse and low frequency pulse. Therefore, during the simulation of double-pulse MIG welding, the welding heat input model could be simplified into periodical changes between intense pulses and weak pulses at a low pulse frequency, as shown in Fig. 4.

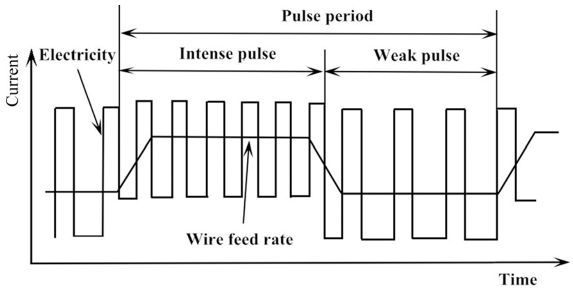

Fig. 4 Schematic diagram of double-pulse MIG welding

The melting and filling processes of the welding wire could be processed using the birth–death element approach. Before the model was solved, weld elements were built in the FEM model, and all weld elements were killed before the heat source was loaded. The so-called killing of elements was executed not to actually delete the elements but to numerically process the elements at the welds. The stiffness and heat transfer matrices of an element were multiplied by a very small coefficient; meanwhile, the specific heat and load vectors were reset to zero. This process was significant to minimize the effect of the death elements whilst ensuring the stability of the stiffness matrix. During the calculation, the death element could be ignored and could not affect the thermal−mechanical coupling process of the welding. As a delivery of heat source, the death elements would be activated at the welding speed. At the same time, the thermophysical and thermodynamic properties of these elements could also be recovered to their original values. This was a process of the material gradually filling into the components.

2.3 Boundary conditions of welding

The initial temperature of the simulation was 30 °C. The details on the relationship between the free surface heat transfer coefficient of 6061-T6 aluminum alloy and the temperature were proposed by ZAIN-UI-ABDEIN et al [9]. During the simulation of the temperature field, a birth−death element technology [10] and a moving heat source were used to simulate the filling and moving of the welding wire. The birth–death elements could be controlled by the model change function in ABAQUS software. After the completion of temperature calculation, the temperature of each node was output as a data file and used as a boundary condition in the calculation of the stress−strain field. During the welding, the crash boxes at two-ends of the cross member completely limited all its degrees of freedom. On the left and right sides of the cross member, the clamp exerted 2 kN downward clamp force. The boundary condition is shown in Fig. 5. The boundary condition of welding was removed after 30 s to simulate the free cooling process of the bumper in the air which was removed from the clamp.

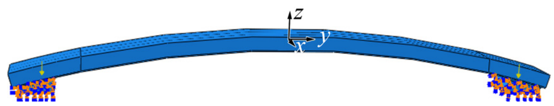

Fig. 5 Bumper displacement boundary condition

2.4 Establishment of bumper finite element model for welding sequence strategy

For the front bumper and crash boxes of the automobile, girth full welding was conducted along the edges of the crash boxes. Eight welds in numbers were produced. The ends of welds were marked with alphabets to distinguish the weld directions, as shown in Fig. 6. According to company requirements, the following four welding sequences were selected:

Solution A: 1(AB)−2(BC)−3(CD)−4(DA)−5(EF)−6(FG)−7(GH)−8(HE);

Solution B: 1(AB)−3(CD)−5(EF)−7(GH)−2(BC)−4(DA)−6(FG)−8(HE);

Solution C: 1(AB)−3(DC)−5(EF)−7(HG)−2(BC)−4(AD)−6(FG)−8(EH);

Solution D: 1(AB)−5(EF)−3(DC)−7(HG)−2(CB)−6(GF)−4(DA)−8(HE).

Solution A was a continuous girth welding sequence where the left crash box was continuously welded firstly and subsequently the right crash box was welded. Three other solutions adopted subsection welding and had certain symmetry. In contrast with Solution D which was symmetrical with the cross beam centre, both Solution B

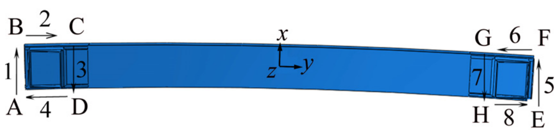

Fig. 6 Schematic diagram of automobile bumper welding sequence

and Solution C were symmetrical with single crash box but were different from the welding directions.

3 Welding process and experimental verification

The double-pulse MIG welding method was used to weld the aluminum alloy bumper. The bumper and the crash boxes were 2 mm-thick 6061-T6 aluminum alloy thin-plate sections. ER5356 aluminum alloy welding wire with a diameter of 1.2 mm was used as the consumable electrode. The chemical composition and mechanical properties of the welded sections and the welding wire were in accordance with the preliminary study [11]. During the welding, the wire extension was 17 mm, the shielding gas was 99.999% argon and the gas flow rate was 25 L/min. The specific technological parameters of the double-pulse MIG welding are shown in Table 1.

Figure 7 shows pictures of the welded structure of the aluminum alloy bumper, which featured a fine overall weld shape along with clear, smooth, good-looking and regular fish scales on the surface. The welds were well fused with the base metal on both sides. These characteristics showed that the welding parameters were reasonable and reliable. The residual stress in the experiment was measured by YC-III stress tester and the strain TJ-120-1.5-Ø1.5 tester (the resistance was 120 Ω), as shown in Fig. 8. The residual stress is expressed as follows [12]:

$$\begin{cases} \sigma_{\text{longitudinal}} = \dfrac{E(\varepsilon_0+\varepsilon_{90})}{4A} - \\ \quad \dfrac{\sqrt{2}E}{4B}\sqrt{(\varepsilon_0-\varepsilon_{225})^2-(\varepsilon_{225}-\varepsilon_{90})^2} \\ \sigma_{\text{horizontal}} = \dfrac{E(\varepsilon_0+\varepsilon_{90})}{4A} + \\ \quad \dfrac{\sqrt{2}E}{4B}\sqrt{(\varepsilon_0-\varepsilon_{225})^2+(\varepsilon_{225}-\varepsilon_{90})^2} \\ \tan 2\alpha = \dfrac{2\varepsilon_{225}-\varepsilon_0-\varepsilon_{90}}{\varepsilon_0-\varepsilon_{90}} \end{cases} \tag{3}$$

where E is the elastic modulus, ε is the strain, α is the direction angle of principal stress, A and B are the stress release coefficients.

$$\begin{cases} A = -\dfrac{1+\mu}{2}\left(\dfrac{r_0}{r}\right) \\ B = -\dfrac{1+\mu}{2}\left[\dfrac{4}{1+r}\left(\dfrac{r_0}{r}\right)^2 - 3\left(\dfrac{r_0}{r}\right)^4\right] \end{cases} \tag{4}$$

Table 1 Double-pulse MIG welding parameters

Average current/A	Average current of intense pulse/A	Average current of weak pulseA	Welding speed/ (cm·min^{-1})	Low pulse frequency/Hz
90	110	70	60	4

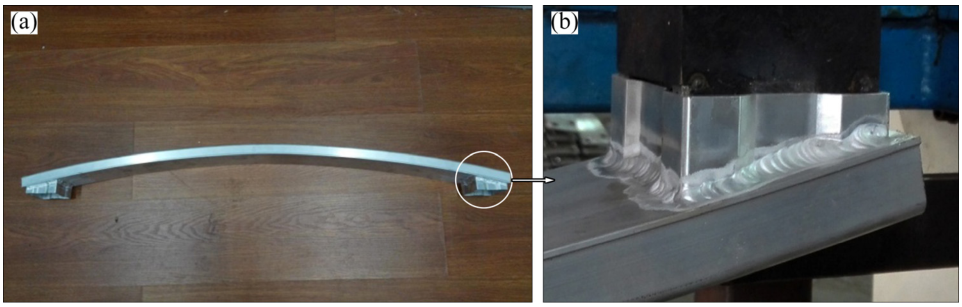

Fig. 7 Pictures of aluminum alloy bumper welding structure: (a) Global structure; (b) Partial enlarged drawing of welding joint

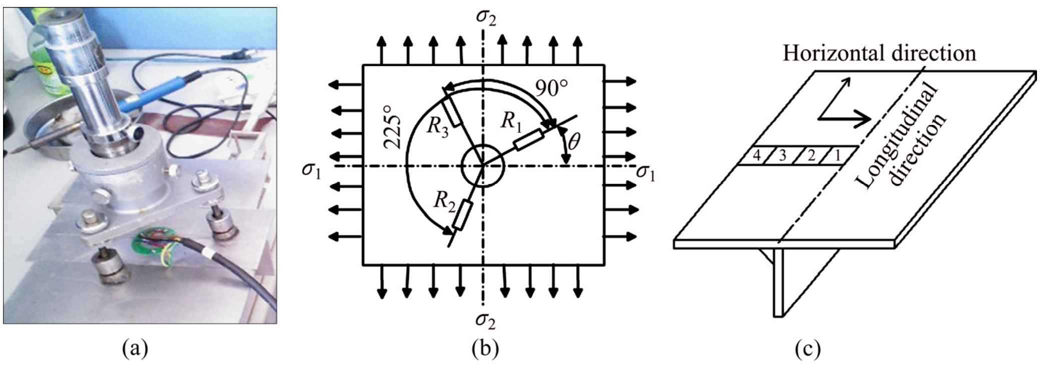

Fig. 8 Details for measurement of residual stress by blind hole method: (a) Equipment drawing; (b) Schematic diagram [12]; (c) Position of strain gauge

where r_0 is the hole diameter and r_0= 0.75 mm, r is the distance from the strain center to the hole center and r=2.5mm. As for 6061 aluminum alloy, elastic modulus E=68.5 GPa, and the Poisson ratio μ=0.33. Then, the stress release coefficient was calculated to be A= −0.0585, B=−0.1642.

The temperature and residual stress of double-pulse MIG welding were simulated on the equal thickness thin-walled T joints with the same welding parameters, which were consistent with the experimental results, as shown in Fig. 9. Both of the temperature and residual stress were reduced when welding along location A to location C. This identity indicated that the simulation was accurate and reliable.

4 Welding simulation analysis

4.1 Welding temperature field of welding

Figure 10 shows the cloud pictures of the temperature field distribution obtained through Solution A. The highest temperature of the fourth weld was 895.9 °C, which was approximately 200 °C higher than the melting point of the base metal, as shown in Fig. 10(b). The heat source zone near the edge of the crash box was characterized by large temperature gradient and dense isotherm distribution, while the isotherm far from the heat source zone was sparse, which conformed to the general law of welding temperature field distribution. The welding temperature distribution of different welds under this welding sequence was basically the same, only the peak temperature was about 914.1 °C, as shown in Fig. 10(c). After welding and cooling for 30 s, the highest temperature of the weld fell to 150.1 °C (Fig. 10(d)). After cooling for 300 s, the highest temperature of the bumper dropped to 42.9 °C (Fig. 10(e)) and most of the zones basically restored to room temperature.

4.2 Stress–strain field of welding

Figure 11 shows the cloud pictures of the stress distribution obtained through Solution A. During the welding of the fourth weld, the metal around the molten

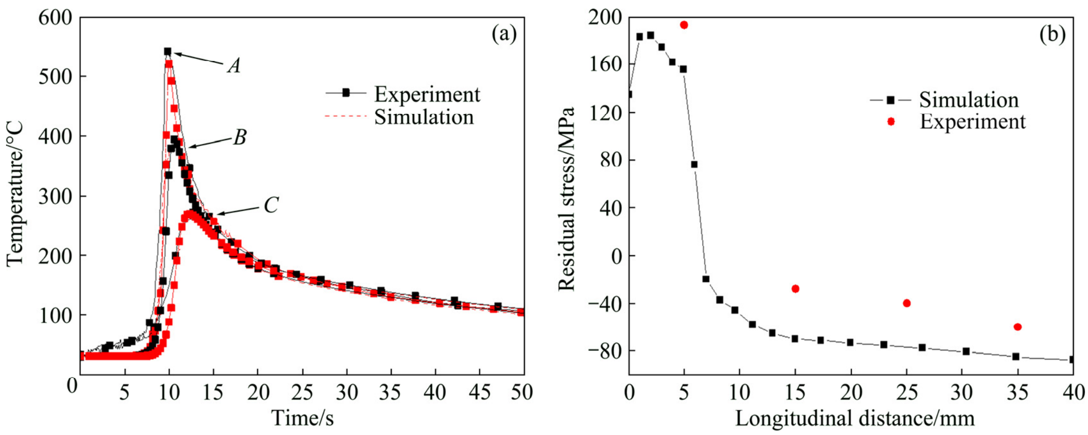

Fig. 9 Comparison between simulation and experiment results of temperature (a) and residual stress along longitudinal direction (b)

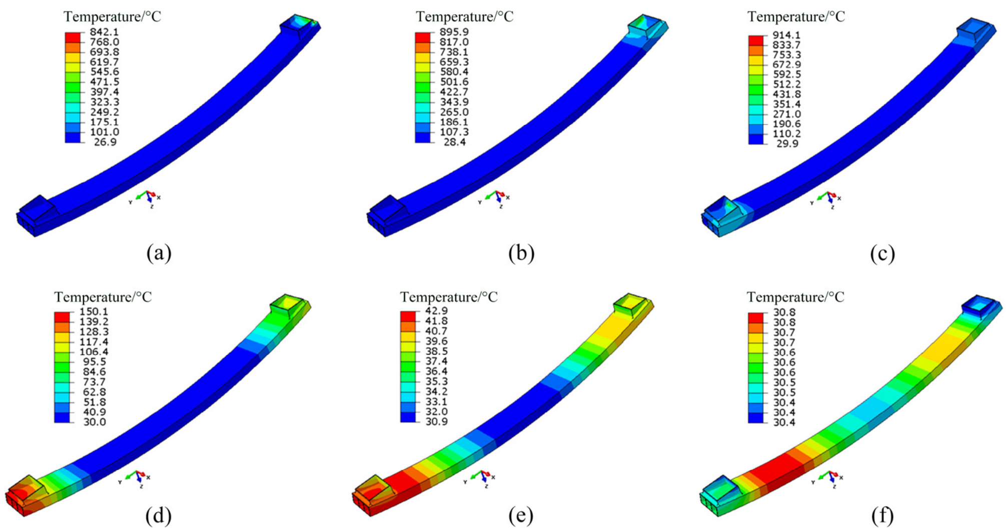

Fig. 10 Cloud pictures automobile bumper welding temperature under different conditions: (a) First weld; (b) Fourth weld; (c) Eighth weld; (d) Cooling for 30 s; (e) Cooling for 300 s; (f) Cooling for 1000 s

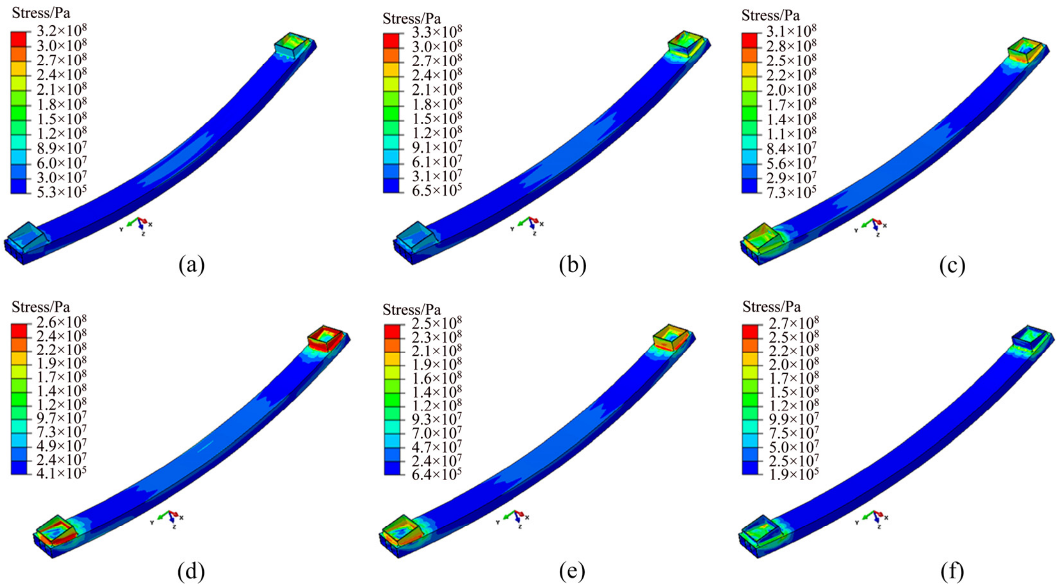

Fig. 11 Cloud pictures automobile bumper welding equivalent stress field under different conditions: (a) First weld; (b) Fourth weld; (c) Eighth weld; (d) Cooling for 30 s; (e) Cooling for 300 s; (f) Cooling for 1000 s

pool was subjected to greater thermal stress, and its value was 330 MPa, exceeding the yield strength of the base metal, as shown in Fig. 11(b). The reason was that aluminum alloy exhibited great thermal conductivity and high linear expansion coefficient. During welding, this metal expanded rapidly due to the heat and produced a compressive plastic deformation of a certain size inside the weld. When welding the eighth weld, the maximum welding heat stresses and their distributions of the eighth and forth welds were not much different because temperature fields of the eighth weld were basically the same as those of the forth weld. After cooling, this compressive plastic deformation still existed so the residual stress was the largest. After cooling for 30 s, the maximum welding stress of the crash box was achieved because the freedom of the crash box was all constrained, as shown in Fig. 11(d). When the component was removed from the welding clamp, the welding residual stress significantly decreased due to the release of the restriction on the crash box. While cooling to room temperature, the welding residual stress of the bumper was mainly concentrated on the crash box and the beam area in the vicinity of the welds. This stress was 273 MPa, which was close to the yield strength of the base metal. This was mainly due to the rapid cooling and contraction of liquid metal near the fillet weld of the beam and the crash box, resulting in the maximum stress near the weld. In addition, the metal near other welds could be deformed freely, while the welding residual stress of the third weld and seventh weld was generally greater than that of other welds due to the mutual restriction of the beam.

After cooling to room temperature, the overall deformation of the bumper was magnified 50 times, as shown in Fig. 12. The welding deformation of the bumper was mainly demonstrated as the contraction of the two ends of the beam and the self-contraction of the crash box influenced by the residual stress. These two phenomena jointly made the distance between the left and right crash boxes increase by 0.94 mm. The left and right crash boxes moved outward by 0.53 mm and 0.41 mm, respectively. The increase of distance greatly aggravated the difficulty of vehicle assembly. Therefore, it is necessary to optimize welding sequence to reduce welding deformation and improve assembly accuracy.

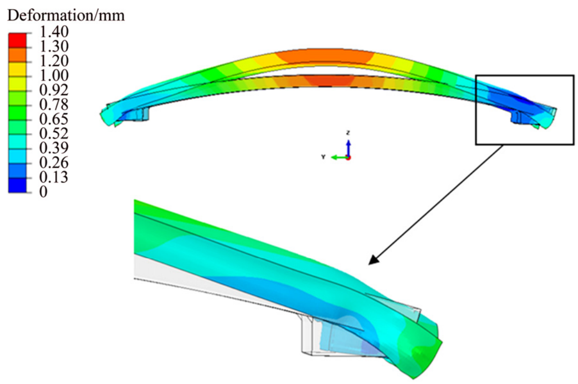

Fig. 12 Simulated results of welding residual deformation for automobile bumper

4.3 Effects of welding sequence on residual stress

The distribution of the welding residual stresses on the bumper showed that the residual stresses on the third weld and the seventh weld were generally larger than those on other welds. Therefore, the residual stress on the third weld was selected to explore the effects of the welding sequence on the bumper welding residual stress. The longitudinal welding residual stress was markedly higher than the transverse one. Thus, the effects of the latter were ignored in this study, and only the effect of the component's longitudinal residual stress on its carrying capacity was analyzed [13].

Figure 13 shows the distribution of the longitudinal residual stresses parallel and vertical to the third weld (along the *x* direction) in four welding sequences. Figure 13(a) shows the residual stress parallel to the third weld. The residual stress changed significantly at the starting and ending points of the welding arc, but that in the middle of the weld was relatively even, mainly because the temperature at the starting and ending points of the welding arc changed markedly. However, the temperature field in the middle was relatively stable. When the weld crater was cooled from a high temperature to room temperature, its residual stress maintained its original uniformity. The variation of residual stress at the starting and ending of the arc was large, but the residual stress in the middle of weld was relatively uniform. This phenomenon was mainly attributed to the large change in the temperature at the starting and ending of the arc, while the temperature field in the middle area was relatively stable. When the molten pool was cooled from high temperature to room temperature, the residual stress remained in the original uniform state. The welding sequence exerted a relatively large effect on the maximum residual stress. The residual stress in Solution A was the smallest, and the maximum residual stress of solution B was smaller than that of Solutions C and D. Figure 13(b) shows the residual stress distribution vertical to the third weld. The maximum tensile stress appeared in the weld centre, and along the direction away from the weld, the tensile stress decreased gradually and changed to the compressive stress subsequently. The largest compressive stress appeared at the centre of the crash box because the contraction of the metal in the surrounding of the weld crater in rapid cooling was restricted by the base metal, resulting in the maximum tensile stress, which was consistent with the stress field distribution. The four welds of the crash box contracted in cooling, which caused the centre of the crash box to generate compressive stress. The stress distribution of the second weld along the *y* direction was largely identical to the longitudinal residual stress distribution, as shown in Fig. 14. By comparing the welding stresses in different welding sequences, the results showed that the welding sequence had little influence on the maximum stress in the weld centre, but had a great influence on the overall stress distribution and size of the welded structure. These results were basically consistent with the research results by JIANG and YAHAOUI [14].

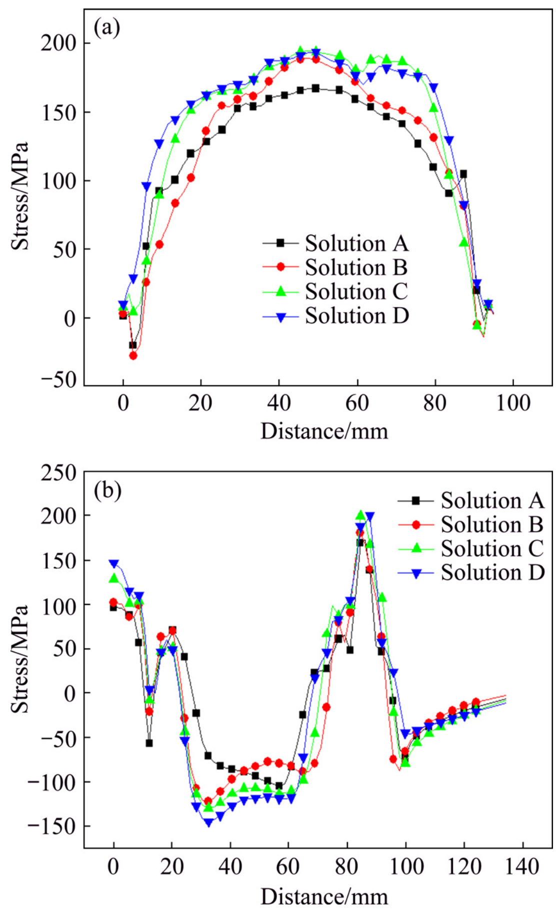

Fig. 13 Stresses along *x* direction of the third weld: (a) Parallel to *x* direction; (b) Vertical to *x* direction

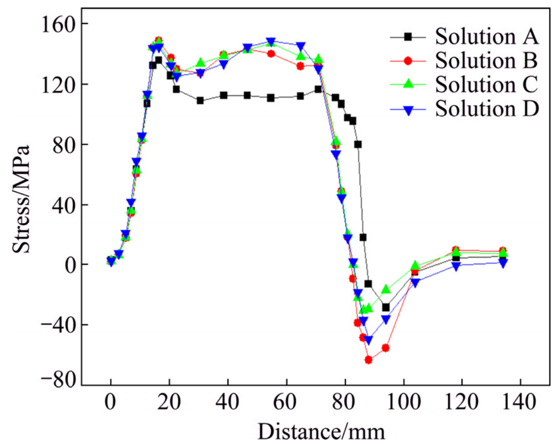

Fig. 14 Stress distributions of the second weld along *y* direction

In conclusion, the residual stress of the weld under solution A was the smallest, followed by that under Solution B, and the stresses generated by Solutions C and D were the largest. When Solution A was used for welding, the temperature of the third weld decreased slowly due to the preheat effect of the second weld and the post-weld heat treatment effect of the forth weld. Accordingly, the residual stress of the third weld was the smallest. Solution B was welded symmetrically in the center of a single crash box. The preheating and post-weld heat treatment effects generated by the welding thermal cycle of adjacent welds were smaller than those under Solution A, so the residual stress was larger than that under Solution A. However, as the heat was not very concentrated, the former weld and the latter weld had little influence on the third weld, so the residual stresses of the two welding sequences were the largest.

4.4 Effects of welding sequence on welding deformation

Table 2 shows the welding heat deformation of the bumper in different welding sequences, including the contraction deformation of the crash box and the largest deformation of the beam along *z* direction.

Table 2 Bumper deformation in different welding sequences

Solution No.	Crash box contraction/mm	Largest deformation along *z* direction/mm
A	0.53	1.43
B	0.50	1.36
C	0.48	1.33
D	0.51	1.40

The welding deformation in Solution A was the largest, while Solutions B and C had the smallest deformation. Therefore, the continuous welding was adopted in Solution A, when the heat concentrated on the unilateral crash box, which made the temperature of the workpiece rise continuously. At the same time, the heat conduction effect of the crash box on the left and right sides was not obvious because of the long beam, and the deformation of the beam was the largest. However, the welding deformations for Solutions B and C with one crash box as the symmetry centre were the smallest because the deformation of the former weld was offset by welding the latter weld when a subsection symmetry welding sequence was adopted. As a result, the relative welding deformation of the workpiece decreased. The symmetry centre adopted in Solution D was the bumper assembly. In the welding process, one weld on the left crash box was welded firstly followed by another one on the right, and this process was repeated. This solution reduced the mutual effect between the two welds. Thus, its welding deformation was smaller than that in Solution A, but larger than that in Solutions B and C. Comparison between Solutions B and C showed that the welding thermal deformation was related to the welding direction in the case of the same welding sequence. In comparison with Solution B of the opposite direction, Solution C of the same welding sequence could reduce the welding deformation greatly.

4.5 Selection of optimal welding sequence

The selection of the optimal welding sequence needs to comprehensively consider the welding residual stress and deformation [15]. Due to the bolted connection between the bumper and the front longitudinal beam, the size accuracy of the bumper is required to be higher, so the increase in distance of the two crash boxes is taken as the first criterion to select welding sequence. In addition, the bumper is the collision safety. The large residual stress on the third weld is likely to tear the beam and the crash box in a collision [16]. Thus, the largest residual stress on the third weld was selected as the second criterion for selecting the welding sequence. The welding deformation results showed that the welding deformations in Solutions A and D were large and did not meet the requirements, whereas the residual stress in Solution C was evidently greater than that in Solution B. Thus, Solution B was optimal. In other words, a reverse symmetry welding with the crash box on one side as the centre could significantly reduce the residual stress of the beam whilst meeting the assembling requirements.

5 Conclusions

(1) The highest temperature in the process of welding the bumper was approximately 200 °C higher than the melting point of the base metal. The welding residual stress of nearly 270 MPa was mainly distributed in the vicinity of the weld between the crash box and the beam. Welding deformation was mainly represented by the contraction of two-ends of the beam and the self-contraction of the crash box under the residual stress. Under the joint effect of these two processes, the distance between the left and right crash boxes was enlarged by 2.05 mm.

(2) The residual stress in Solution A was the smallest, while the residual stresses generated by Solutions C and D were the largest. The welding deformation in Solution A was the largest, while deformations in Solutions B and C were the smallest and there was little difference between them.

(3) Considering the influence of welding residual stress and deformation on the assembly and structure properties, the optimal sequences was Solution B in which a single crash box was welded symmetrically in opposite direction, which can effectively reduce residual stress and meet the assembly requirements.

References

[1] LIU Hai-jiang, ZHANG Xia, XIAO Li-fang. Collision simulation analysis of 7075 aluminum alloy car bumper based on LS-DYNA [J]. Journal of Machine Design, 2011, 28: 18−23.

[2] WAN Yin-hui, WANG Guan, LIU Zhi-wen, ZHOU Jia, LI Luo-xing. Crash properties of 6061 aluminum alloy bumper beam [J]. Materials

for Mechanical Engineering, 2012, 36: 67−71.
[3] IMAM FAUZI E R, CHE JAMIL M S, SAMAD Z, MUANGJUNBUREE P. Microstructure analysis and mechanical characteristics of tungsten inert gas and metal inert gas welded AA6082-T6 tubular joint: A comparative study [J]. Transactions of Nonferrous Metals Society of China, 2017, 27: 17−24.
[4] WANG Bo, XUE Song-bai, MA Chao-li, HAN Yi-long, LIN Zhong-qiang. Effect of combinative addition of Ti and Sr on modification of AA4043 welding wire and mechanical properties of AA6082 welded by TIG welding [J]. Transactions of Nonferrous Metals Society of China, 2017, 27: 272−281.
[5] SATTARI-FAR I, JAVADI Y. Influence of welding sequence on welding distortions in pipes [J]. International Journal of Pressure Vessels and Piping, 2008, 85: 265−274.
[6] FU Ding-fa, ZHOU Chang-qing, LI Can, WANG Guan, LI Luo-xing. Effect of welding sequence on residual stress in thin-walled octagonal pipe-plate structure [J]. Transactions of Nonferrous Metals Society of China, 2014, 24: 657−664.
[7] GOLDAK J, CHAKRAVARTI A, BIBBY M. A new finite element model for welding heat sources [J]. Metallurgical Transactions B, 1984, 15: 299−305.
[8] FANG Hong-yuan, MENG Qing-guo, XU Wei-li, JI Shu-de. New general double ellipsoid heat source model [J]. Science and Technology of Welding and Joining, 2005, 10: 361−368.
[9] ZAIN-UI-ABDEIN M, NELIAS D, JULLIEN J F, DELOISON D. Experimental investigation and finite element simulation of laser beam welding induced residual stresses and distortions in thin sheets of AA 6056-T4 [J]. Materials Science and Engineering A, 2010, 527: 3025−3039.
[10] AKBARI MOUSAVI S A A, MIRESMAEILI R. Experimental and numerical analyses of residual stress distributions in TIG welding process for 304L stainless steel [J]. Journal of Materials Processing Technology, 2008, 208: 383−394.
[11] YI Jie, CAO Shu-fen, LI Luo-xing, GUO Peng-cheng, LIU Kai-yong. Effect of welding current on morphology and microstructure of Al alloy T-joint in double-pulsed MIG welding [J]. Transactions of Nonferrous Metals Society of China, 2015, 25: 657−664.
[12] FEJA K, HAUK V, KRUG W K, PINTSCHOVIUS L. Residual stress evaluation of a cold-rolled steel strip using X-rays and a layer removal technique [J]. Materials Science and Engineering A, 1987, 92: 13−21.
[13] CAO Shu-fen, CHEN Tie-ping, YI Jie, GUO Peng-cheng, LI Luo-xing. Simulation of temperature, stress and deformation during [J]. The Chinese Journal of Nonferrous Metals, 2014, 24: 1685−1692. (in Chinese)
[14] JIANG W, YAHAOUI K. Effect of welding sequence on residual stress distribution in a multipass welded piping branch junction [J]. International Journal of Pressure Vessels and Piping, 2012, 95: 39−47.
[15] CHANG K H, LEE C H. Effect of the welding sequence in the circumferential direction on residual stress distribution in a thin-walled pipe weld [J]. Journal of Engineering Manufacture, 2009, 223: 723−735.
[16] DEB A, MAHENDRAKUMAR M S, CHAVAN C, KARVE J, BLANKENBURG D, STOREN S. Design of an aluminum-based vehicle platform for front impact safety [J]. International Journal of Impact Engineering, 2004, 30: 1055−1079.

焊接顺序对 6061-T6 铝合金汽车结构件焊接残余应力及变形的影响

易 杰 [1,2,3]，张见明 [1,3]，曹淑芬 [1,3]，郭鹏程 [1,3]

1. 湖南大学 汽车车身先进设计与制造国家重点实验室，长沙 410082；
2. 湖南工业职业学院 机械工程学院，长沙 410208；
3. 湖南大学 机械与运载工程学院，长沙 410082

摘 要：采用 ABAQUS 软件中的非线性弹塑性有限元方法，对 6061-T6 铝合金汽车保险杠进行 4 种不同的双脉冲 MIG 焊接顺序试验。在 4 种焊接顺序下焊接后的残余应力和变形均有明显差异。结果表明，在方案 A 中，最高温度高于基体金属的熔点约 200 °C。这种大的温度梯度导致较高残余应力，且残余应力主要集中在横梁与吸能盒的焊缝附近。焊接变形主要是由于横梁两端的收缩和吸能盒的自收缩。与其他焊接顺序相比，方案 A 中残余应力最小，焊接变形最大。然而，由于方案 B 有效地降低了残余应力和满足良好的装配要求，因此，方案 B 是本研究得到的最优焊接方案。

关键词：双脉冲 MIG 焊接；焊接顺序；焊接残余应力；焊接变形；最优方案

(Edited by Wei-ping CHEN)